Supporting Information

Petrinovic et al. 10.1073/pnas.1214255110

SI Materials and Methods

Animals. Nogo-A knockout (KO) [pure C57BL/6 background; postnatal day (P) 4-60] and transgenic mice overexpressing Nogo-A exclusively in Purkinje cells (PC) under the L7 promoter (L7–Nogo-A TG) (in FVB/N background; P4-P60) were used in this study. Wild-type (WT) mice of both C57BL/6 and FVB/N strains were used as respective controls. All animal experiments were performed according to the guidelines of the Veterinary Office of the Canton of Zürich, Switzerland, and approved by its Commission for Animal Research. All efforts were made to minimize animal suffering and to reduce the number of animals required.

Nogo-A KO mice were generated by homologous recombination of exons 2 and 3 in the Nogo-A gene as described previously (1). Animals were backcrossed with C57BL/6 WT mice for more than 10 generations resulting in strain purity of > 99.98% (2). The backcrossed heterozygous mice were then bred to get homozygous WT or KO mice. The generation of transgenic mice overexpressing Nogo-A under the cerebellar PC-specific L7 promoter (3, 4) has been previously described (5). In this study we used line 24 in which the rat Nogo-A transgene is expressed in all cerebellar PCs.

Antibodies. For immunohistochemical detection of Nogo-A we used the polyclonal rabbit antibody Rb173A (Laura, 1:200), which recognizes the Nogo-A–specific region (amino acids 174–979) (6, 7). The polyclonal rabbit antibody Rb1 (Bianca) which is specific for the N terminus of Nogo-A and Nogo-B (amino acids 1–172, 1:15,000) (6, 7) was used for immunodetection of these two proteins in cerebellar lysates. Monoclonal antibody 3D11, which recognizes the C-terminal part of a rat but not mouse Nogo-A–specific region (amino acids 910–920, 1:50) (7) was used for the detection of the transgene in L7–Nogo-A TG mice. Polyclonal goat antibody against NgR1 (R&D Systems; 1:500) was used for detection of this Nogo-A receptor and anti-calbindin D-28k (Swant; 1:500) antibody was used for immunohistochemical identification of PCs. Anti-vesicular glutamate transporter 1 (VGluT1) antibody (Synaptic Systems; 1:1,000) and anti-vesicular glutamate transporter 2 (VGluT2) antibody (Synaptic Systems; 1:1,000) were used for immunohistochemical identification of parallel (PF) and climbing fiber (CF) terminals, respectively, as well as for identification of respective proteins in cerebellar tissue lysates. Antibodies against CaMKII (Upstate; 1:1,000), PSD95 (Abcam; 1:1,000), SNAP25 (Chemicon; 1:500), GluR2/3 [gift from P. Streit (Brain Research Institute, University of Zurich, Zurich, Switzerland); 1:500], GluR1 (gift from P. Streit; 1:500), phospho-PKCγ (Abcam; 1:1,000), and Homer (Synaptic Systems; 1:500) were used for detection of these proteins in cerebellar tissue lysates. Monoclonal antiglyceraldehyde-3-phosphate dehydrogenase (GAPDH) antibody served as a protein loading control on Western blots (Abcam; 1:10,000).

The following secondary antibodies were used: horseradish peroxidase (HRP)-conjugated goat anti-mouse IgG (Pierce; 1:15,000), HRP-conjugated donkey anti-rabbit IgG (Pierce; 1:10,000), HRP-conjugated mouse anti-goat IgG (Pierce; 1:10,000), Cy3-coupled goat anti-rabbit IgG (Jackson ImmunoResearch Laboratories; 1:3,000), Cy3-coupled goat anti-mouse IgG (Jackson ImmunoResearch Laboratories; 1:2,000), Cy2-coupled goat anti-mouse IgG (Jackson ImmunoResearch Laboratories; 1:2,000), Cy3-coupled mouse anti-goat IgG (Jackson ImmunoResearch Laboratories; 1:3,000), and DyLight 640 streptavidin (Jackson ImmunoResearch Laboratories; 1:1,000).

Immunoblotting. Mice were killed by cervical dislocation and the cerebella were quickly removed and sectioned into 400-μm thick sagittal slices using a McIlwain tissue chopper. The slices were then submerged in ice-cold phosphate buffer (pH 7.4), the deep white matter was removed, and the molecular layer was then quickly hand dissected under a dissection microscope (8) and subsequently flash frozen in liquid nitrogen. The tissues were then stored at −80 °C until extraction in lysis buffer (50 mM NaH_2PO_4, 150 mM NaCl, 0.5% CHAPS, pH 8.0) containing protease inhibitors (Complete Mini; Roche Diagnostics). After homogenization, samples were centrifuged for 15 min at 2,000 × *g* at 4 °C, and the protein concentration of the supernatant was determined using NanoDrop ND 1000 (NanoDrop Technologies, ThermoFisher Scientific). Protein samples (30 μg) were separated by electrophoresis on 4–12% NuPAGE gels (Invitrogen) and electroblotted to polyvinylidene difluoride membranes (Millipore). Membranes were incubated in 3% (wt/vol) Top Block (Lubio Science)/0.1% TBST (0.1 M Tris base, 0.1% Tween 20, pH 7.4) for 1 h at room temperature, followed by incubation with primary antibodies overnight at 4 °C. Immunoreactivity was visualized using HRP-conjugated secondary antibodies and a chemiluminiscent substrate (SuperSignal West Pico; Pierce). Images were captured with the Stella system (Rytest) and densitometry analysis was performed with ImageJ software (National Institutes of Health, NIH). Quantification was done by normalizing the protein band intensities to GAPDH values.

Immunohistochemistry. Mice were deeply anesthetized with pentobarbital (Nembutal, 75 mg/100 g body weight; Abbott Laboratories) and transcardially perfused with PBS (pH 7.4), followed by 4% (wt/vol) paraformaldehyde (PFA)/0.05% glutaraldehyde solution in PBS. The cerebella were then removed and postfixed in 4% PFA either overnight (P14–P60 mice) or for 2 d (P4–P7 mice). After cryoprotection in 30% (wt/vol) sucrose the cerebella were rapidly frozen on dry ice and stored at −80 °C. Forty-micrometer-thick sagittal sections were cut on a cryostat and collected in cold PBS. Tissue sections were stained with Cresyl violet, and images were taken with a Zeiss Axiophot microscope equipped with a cooled CCD camera (CoolSNAP HQ; Photometrics). For immunofluorescence, free floating tissue sections were permeabilized and nonspecific protein interactions were reduced by incubation in a blocking buffer [4% (vol/vol) normal goat serum, 0.3% Triton X-100 in TBS, pH 8.0] for 30 min at room temperature. Primary antibodies were applied overnight at 4 °C and after washing with TBS, sections were incubated with the appropriate secondary antibody for 2 h at room temperature. Finally, sections were mounted on Superfrost-Plus slides (Menzel-Gläser) and coverslipped with Mowiol.

Epifluorescence images were acquired with a cooled CCD camera (CoolSNAP HQ; Photometrics) coupled to a Zeiss Axiophot microscope interfaced by the MCID/M2 Imaging System (Imaging Research). A 5× objective (PLAN NEOFLUAR, NA 0.15) was used. Confocal imaging was performed by using a Spectral Confocal Microscope TCS SP2 AOBS (Leica) and a 5× (HC PL FLUOTAR, NA 0.15), 20× (HC PL FLUOTAR, NA 0.50), and a 63× oil immersion objective (HCX PL APO Oil, NA 1.32). The pinhole was set at 1 Airy unit. Double-immunofluorescence staining was visualized with sequential acquisition of separate color channels to avoid cross-talk between fluorochromes.

Quantitative Measurements and Data Analysis. As the cerebellar lobules, and even different regions of the same lobule, mature at different time points (9), and as the CF innervation of PCs in the sulcus is different from that in the bank and gyrus subdivisions (10), we analyzed the bank and gyrus regions of the lobules IV/V, VI/VII, and IX in each animal. Quantification was done in a blind manner with respect to the genotypes.

To evaluate quantitative differences in CF extensions between normal and mutant cerebella, we measured the distance from the base of the molecular layer to the most distal tips of continuous VGluT2 immunopositive puncta, which ascended along the dendritic tree of a given PC, relative to the vertical length of the entire molecular layer. Furthermore, to estimate the translocation of CFs from the soma to dendrites of PCs, they were divided into three categories: PCs without $VGluT2^+$ CF varicosities on their soma, PCs with one to five $VGluT2^+$ CF terminals, and PCs with more than six $VGluT2^+$ CF varicosities. The sample size was: WT/BL6 (n = 120 cells from six mice), Nogo-A KO (n = 126 cells from six mice), WT/FVB (n = 132 cells from six mice), and L7–Nogo-A TG (n = 127 cells from six mice).

For quantification of $VGluT1^+$ and $VGluT2^+$ terminals, confocal imaging was performed by using a Spectral Confocal Microscope TCS SP2 AOBS (Leica) and a 63× oil immersion objective (HCX PL APO Oil, NA 1.32). Confocal image acquisition consisted of 12 images in the z dimension with a step size of 0.7 μm and image size of 0.36 μm per pixel (1,024 × 1,024). Double-immunofluorescence staining was visualized with sequential acquisition of separate color channels to avoid cross-talk between fluorochromes. Quantification of $VGluT1^+$ and $VGluT2^+$ terminals was done by using ImageJ software (NIH). The sample size for VGluT1 was: WT/BL6 (n = 118 cells from six mice), Nogo-A KO (n = 129 cells from six mice), WT/FVB (n = 145 cells from six mice), and L7–Nogo-A TG (n = 133 cells from six mice); the sample size for VGluT2 was: WT/BL6 (n = 105 cells from six mice), Nogo-A KO (n = 116 cells from six mice), WT/FVB (n = 114 cells from six mice), and L7–Nogo-A TG (n = 103 cells from six mice).

Acute Cerebellar Slices. Acute cerebellar slices were prepared from P28 mice anesthetized with Halothane (Sigma). After decapitation, the vermis was removed and mounted in a chamber filled with cooled (0–3 °C) extracellular solution containing the following (mmol): 120 NaCl, 26 $NaHCO_3$, 2 KCl, 2 $CaCl_2$, 1.19 $MgSO_4$, 1.18 NaH_2PO_4, and 11 glucose (osmolarity 285–295 mosmol/kg, pH 7.4 when equilibrated with 95% O_2–5% CO_2). The 225-μm-thick slices were cut using a VT1000S slicer (Leica Instruments) and incubated in oxygenated extracellular solution at 32 °C for at least 30 min before they were transferred to the recording chamber mounted on the stage of an upright microscope (Zeiss; Axioskop 2) where they were continuously perfused with oxygenated extracellular solution at room temperature. Midsagittal slices were used for all of the experiments except for those requiring PF stimulation for which horizontal slices were used. For the study of excitatory synaptic transmission, 20 μM picrotoxine (Sigma) was added to the extracellular medium. PCs were visually identified and recorded using the perforated-patch configuration of the patch clamp technique (11).

Electrophysiology. Patch pipettes were made of borosilicate glass (Hilgenberg) with resistances of 2–6 MΩ when filled with the patch pipette solution containing the following (mmol): 80 K_2SO_4, 10 NaCl, 15 glucose, 5 Hepes (osmolarity 230 mosmol/kg, pH adjusted to 7.2 with KOH). Recordings were performed for both current- and voltage-clamp modes using an EPC 10 amplifier (HEKA) or an Axopatch 500B (Molecular Devices) with an ITC16 analog-to-digital converter (Instrutech) and an 8-pole analog Bessel low-pass filter (Frequency Devices). All current-clamp recordings were made using the fast current-clamp mode of the amplifiers. Stimulus generation and data acquisition were made with Pulse 8.65 software (HEKA). Spontaneous and depolarization-evoked potential signals were filtered at 4 kHz and digitally sampled at 20 kHz. Evoked postsynaptic currents were filtered at 2 kHz and digitally sampled at 10 kHz. Evoked postsynaptic potentials (complex spikes) were filtered at 20 kHz and digitally sampled at 100 kHz.

Spontaneous action potential firing frequency was analyzed from current-clamp recordings. Intrinsic excitability was investigated by setting the membrane potential at −80 mV and injecting 1-s steps of depolarizing current (from 0 to 2.5 nA in 50-pA increments). When injected with sufficient depolarizing current, PCs generated repetitive spikes. Action potential frequency was measured as the action potential frequency remains stable for a given injected current intensity. The average frequency over the time of current injection was measured by dividing the number of interspike intervals by the time interval between the first and the last spike. These values were used to construct current–frequency plots. A close-to-linear relationship between frequency and current is observed (12). The slope of the first six points of the current–frequency curve was used as a measure of the intrinsic cell excitability. The sample size was: WT/BL6 (n = 21 cells from four mice), Nogo-A KO (n = 25 cells from six mice), WT/FVB (n = 24 cells from six mice), and L7–Nogo-A TG (n = 26 cells from five mice).

Parallel fiber stimulation. For PF stimulation, a patch pipette filled with 0.9% NaCl was placed in the molecular layer at about two-thirds of the distance between the PC layer and the pial surface. The holding potential was set at −90 mV. Negative current pulses ranging from 0 to 8 μA with duration of 150 μs were delivered in ascending order with 1-μA increments at 5-s intervals. These pulses were generated by an Iso-flex stimulus isolation unit (AMPI) driven by a programmable Master 8 Stimulator/Pulse generator (AMPI) synchronized with data acquisition through Pulse software. PF excitatory postsynaptic currents (EPSCs) were identified by their characteristic features (graded response amplitude and paired-pulse facilitation) (13). EPSC amplitude was measured as the difference between the current baseline level before the stimulus artifact and the peak of the EPSC. For each stimulus intensity, a single EPSC value was calculated as the mean of three successive evoked responses. Linear fits were obtained from EPSC slope values in each cell for the first eight points of the stimulus–response curve. Input–output relations measuring EPSC initial slope (pA/ms, output) as a function of PF stimulus intensity (μA, input) were established for each recorded neuron. Because this relation is linear, we used the mean linear slope factor for the first eight points of the stimulus–response curve to compare the synaptic strength of the PF–PC synapse. Paired-pulse facilitation (PPF) was elicited by twin pulses at different time intervals (5–245 ms by 2-ms increments) as previously described (14). A single EPSC value was calculated as the mean of five successive evoked responses. PPF ratio was expressed as the difference between the second and the first EPSC divided by the size of the first EPSC. To elicit CF responses, the stimulating micropipette was placed in the granule cell layer and moved in the vicinity of the recorded PC until the typical response characterized by multiple wavelets (complex spike) was obtained. The membrane potential was set at –90 mV with constant current injection. The sample size was: WT/BL6 (n = 23 cells from four mice), Nogo-A KO (n = 20 cells from six mice), WT/FVB (n = 19 cells from five mice), and L7–Nogo-A TG (n = 25 cells from four mice).

Climbing fiber stimulation. PCs were patched with a patch pipette (2–4 MΩ) filled with a solution containing (mmol): 100 CsCl, 35 Cs-sulfonate, 11 Tris·phosphocreatine, 10 Hepes, 4.5 Mg ATP, 0.3 Tris·GTP, (osmolarity: 298 mosmol, pH adjusted to 7.25 with NaOH). To inactivate voltage-dependent conductances and to reduce the driving force and current amplitudes, the holding

potential was set at −10 mV. For CF stimulation, a patch pipette (1 MΩ) filled with artificial cerebrospinal fluid (CSF) was placed in the granule cell layer, in the vicinity of the PC, and moved until the CF response could be elicited with a minimal stimulus intensity. Two current pulses (0.1 ms, paired-pulse interval: 100 ms) were applied every 20 s. These pulses were generated by a stable IS4 stimulator (SC Devices). Subsequently, the stimulus intensity was lowered until all synaptic responses disappeared, then increased again and the increase in the synaptic response as a function of the stimulus intensity was analyzed. Only events with a clear threshold and showing paired-pulse depression were counted as CF responses. Cells with a single threshold were classified as monoinnervated, whereas cells with more than one threshold event were classified as polyinnervated. The sample size for P14 was: WT/BL6 (n = 26 cells from six mice), Nogo-A KO (n = 29 cells from eight mice); and for P28: WT/BL6 (n = 28 cells from eight mice) and Nogo-A KO (n = 30 cells from seven mice).

Morphological Reconstruction of Single Purkinje Cells. In a separate series of whole-cell recordings used for morphological reconstruction, the intracellular solution contained (mmol): 126 K gluconate, 0.05 $CaCl_2$, 0.15 BAPTA, 4 NaCl, 1 $MgSO_4$, 15 glucose, 5 Hepes, 3 Mg ATP, 0.1 GTP (pH adjusted to 7.2 with KOH), and 0.4% biocytin (Sigma). Granule cell migration, which defines the depth of the molecular layer, was always complete. Purkinje cells, situated in the bank and gyrus regions of lobules IV/V, VI/VII, and IX, were filled with biocytin during 15 min and fluorescence was subsequently revealed by cytochemistry. To this end, slices were fixed by immersion in 4% PFA overnight and biocytin was revealed with streptavidin-conjugated fluorescein isothiocyanate (FITC, Jackson Immunoresearch; 1:200). After three rinses in TBS, slices were mounted on coverslips with "Slow Fade Light" (Invitrogen) mounting medium in 50% (vol/vol) glycerol and secured with nail polish. Images of the fluorescent cells were acquired using a LSM 510 META laser scanning confocal system (Zeiss) mounted on an Axiovert 200M inverted microscope (Zeiss) equipped with c-Achroplan NIR 40×/0.8 W objective (Zeiss). Images of the dendritic endings were acquired on the same system with a c-Apochromat 63×/1.2 W objective (Zeiss). The excitation beam of an Argon laser (488 nm) and band-pass emission filters (500–550 nm) were used for selective detection of the green fluorochrome. Sequential optical sections of 2048 × 2048 pixels were taken at 1.0-μm intervals along the z axis to allow 3D reconstruction. Possible distortion caused by the histological processing has been shown to cause less than 5% error on estimated length (15). Data acquisition and analysis were performed in a blind manner with respect to the genotypes. The sample size for quantitative image analysis was: WT/BL6 (n = 14 cells from 3 mice), Nogo-A KO (n = 24 cells from four mice), WT/FVB (n = 11 cells from four mice), L7–Nogo-A TG (n = 18 cells from three mice).

Morphometric Analysis of Purkinje Cell Dendrites and Spines. Cellular volumes were computed by evaluating the number of voxels inside the cells. For each cell, the threshold value defining the cell surface was set using the ISODATA algorithm implemented in ImageJ software (NIH). The total number of voxels inside the cell was then evaluated using the VoxelCounter plugin for ImageJ software (NIH) and multiplied by the unitary voxel volume. 2D fractal dimensions were obtained on z-projections with the box counting method using the FracLac 2.3 plugin for ImageJ software (NIH).

Due to the complexity of the PC dendritic tree, the skeletonization algorithms available in existing software (Imaris, Neurolucida) give unreliable results and do not allow a quantitative analysis of the dendritic structure. Therefore, we have chosen to use the computation of the fractal dimension as a measure of the overall complexity of the object in 2D images obtained by doing z-projections of the images stacks. Neurons can indeed be represented as fractal or space-filling objects and the fractal dimension represents a very good parameter for the characterization of the dendritic structure (16–20). Furthermore, as shown by Jelinek and Fernandez (19), the shrinkage or expansion of a neuron due to the experimental manipulation will not affect their fractal values as long as the artifact acts equally in all directions and the measured points still lie on the linear segment of the graph. Therefore, fractal dimensions of different neurons that have been processed in different batches or at different laboratories can be compared directly if the same methodology for calculating fractal dimensions is applied.

The average width of distal dendritic segments was evaluated by measuring the apparent area in z-projection. Dendritic spine number per unit length (spine density) was counted on z-projections and divided by the length of the dendrites. The sample size was: WT/BL6 (n = 14 cells from 3 mice), Nogo-A KO (n = 24 cells from 4 mice), WT/FVB (n = 11 cells from four mice), L7–Nogo-A TG (n = 18 cells from three mice).

Anterograde Tracing of Climbing Fibers. The anterograde tracing of CFs was performed in P7 and P21 WT/BL6 and Nogo-A KO mice as described previously (21, 22). P7 animals were placed on ice for 4.5 min to induce anesthesia by hypothermia. P21 mice were anesthetized with a s.c. injection of Hypnorm (0.047 mg/100 g, VetaPharma) and Dormicum (1.5 mg/100 g, Roche Diagnostics). Animals were mounted in a rodent stereotaxic frame and the cerebellomeduallary cistern was identified by palpation. After opening the skin, muscle layers and connective tissue were opened along the sagittal midline leaving the ligament intact. A 10-μL NanoFil syringe with a 33 gauge bevelled needle (World Precision Instruments) was aligned to the occipital bone at the cerebellomedullary cistern. The needle was then slowly lowered to a final depth of 2.5–2.7 mm bellow the ligament in P7 animals and to 2.7–3.0 mm in P21 mice. By moving the needle slowly down and constantly observing the skull and the needle shaft we identified the depth of the floor of the occipital bone. The needle was then retracted for 0.3 mm from the ventral surface and 1 μL of 10% (vol/vol) biotinylated dextran amine (BDA) (Invitrogen) solution was slowly injected (50 nL/s). After being kept in place for additional 2 min, the needle was slowly retracted and the wound was closed with Histoacryl (BBraun). Seven days after the surgery, animals were perfused with 4% (wt/vol) PFA and the brains were collected and processed for immunohistochemistry (as described above). After staining with anticalbindin and anti-VGluT2 antibodies (as described in *Immunohistochemistry*), tissue sections were stained for 30 min with Cy5-conjugated streptavidin to visualize the BDA-labeled CFs. The sample size for quantitative image analysis for P14 was: WT/BL6 (n = 24 cells from five mice), Nogo-A KO (n = 21 cells from four mice); and for P28: WT/BL6 (n = 21 cells from six mice) and Nogo-A KO (n = 19 cells from four mice).

Electron Microscopy. Mice were deeply anesthetized with pentobarbital (Nembutal, 75 mg/100 g body weight; Abbott Laboratories) and transcardially perfused with 0.1 M PBS (pH 7.4), followed by 4% (wt/vol) PFA/0.05% glutaraldehyde solution in 0.1 M PBS (pH 7.4). The cerebella were dissected and postfixed in the same solution for 4 h. Forty-micrometer-thick parasagittal sections were cut on a cryostat and postfixed in 2% (wt/vol) OsO_4 at 4 °C for 1 h (23). After dehydration in ethanol, the sections were contrasted in 0.5% uranyl acetate in 95% (vol/vol) ethanol for 1 h and embedded in Epon. Ultrathin sections of 80 nm were analyzed in a Zeiss EM10 electron microscope. Excitatory synapses were identified in electron micrographs as mushroom-shaped spines containing a postsynaptic density (PSD) juxtaposed to a presynaptic terminus with associated synaptic vesicles according to previously described criteria (23). PSD length of at

least 70 spines per animal was determined in the upper half of the molecular layer by using ImageJ software (NIH). All measurements were made by an experimenter blinded to the sample identity.

For immunolocalization of Nogo-A and NgR1, 50-μm-thick cerebellar cryosections were treated with freshly made 0.5% $NaBH_4$ in TBS for 10 min to reduce the background staining. Sections were then rinsed several times in TBS and incubated overnight with the primary antibody (Laura, 1:200; NgR1, 1:500). Sections were subsequently treated with 0.025% 3,3′-diaminobenzidine tetrahydrochloride (DAB) in the presence of 0.006% H_2O_2 for 15 min. DAB staining was subsequently intensified by methenamine silver-gold reaction according to the protocol of Teclemariam-Mesbah et al. (24). The high electron density of gold-substituted silver grains facilitates ultrastructural recognition of stained structures. Finally, sections were osmicated, embedded in Epon, and ultrathin sections of 100 nm were analyzed in a Zeiss EM10 electron microscope.

Statistical Analysis. All data are shown as mean values ± SEM and considered significant at a level of $P < 0.05$. Two-way ANOVA test was used for comparison of paired-pulse facilitation data, whereas the significance between groups in all of the other measurements was calculated using Student's t test. Graphs were generated using GraphPad Prism. The levels of significance are indicated as follows: $^{*}P < 0.05$, $^{**}P < 0.01$, $^{***}P < 0.001$.

1. Simonen M, et al. (2003) Systemic deletion of the myelin-associated outgrowth inhibitor Nogo-A improves regenerative and plastic responses after spinal cord injury. *Neuron* 38(2):201–211.
2. Dimou L, et al. (2006) Nogo-A-deficient mice reveal strain-dependent differences in axonal regeneration. *J Neurosci* 26(21):5591–5603.
3. Oberdick J, Smeyne RJ, Mann JR, Zackson S, Morgan JI (1990) A promoter that drives transgene expression in cerebellar Purkinje and retinal bipolar neurons. *Science* 248 (4952):223–226.
4. Smeyne RJ, et al. (1991) Dynamic organization of developing Purkinje cells revealed by transgene expression. *Science* 254(5032):719–721.
5. Aloy EM, et al. (2006) Synaptic destabilization by neuronal Nogo-A. *Brain Cell Biol* 35 (2-3):137–156.
6. Dodd DA, et al. (2005) Nogo-A, -B, and -C are found on the cell surface and interact together in many different cell types. *J Biol Chem* 280(13):12494–12502.
7. Oertle T, et al. (2003) Nogo-A inhibits neurite outgrowth and cell spreading with three discrete regions. *J Neurosci* 23(13):5393–5406.
8. Sandoval ME, Cotman CW (1978) Evaluation of glutamate as a neurotransmitter of cerebellar parallel fibers. *Neuroscience* 3(2):199–206.
9. Altman J (1972) Postnatal development of the cerebellar cortex in the rat. I. The external germinal layer and the transitional molecular layer. *J Comp Neurol* 145(3): 353–397.
10. Nishiyama H, Linden DJ (2004) Differential maturation of climbing fiber innervation in cerebellar vermis. *J Neurosci* 24(16):3926–3932.
11. Horn R, Marty A (1988) Muscarinic activation of ionic currents measured by a new whole-cell recording method. *J Gen Physiol* 92(2):145–159.
12. Llinás R, Sugimori M (1979) Calcium conductances in Purkinje cell dendrites: Their role in development and integration. *Prog Brain Res* 51:323–334.
13. Konnerth A, Keller BU, Lev-Tov A (1990) Patch clamp analysis of excitatory synapses in mammalian spinal cord slices. *Pflugers Arch* 417(3):285–290.
14. Sacchetti B, Scelfo B, Tempia F, Strata P (2004) Long-term synaptic changes induced in the cerebellar cortex by fear conditioning. *Neuron* 42(6):973–982.
15. Roth A, Häusser M (2001) Compartmental models of rat cerebellar Purkinje cells based on simultaneous somatic and dendritic patch-clamp recordings. *J Physiol* 535(Pt 2): 445–472.
16. Alves SG, Martins ML, Fernandes PA, Pittella JEH (1996) Fractal patterns for dendrites and axon terminals. *Physica A* 232(1-2):51–60.
17. Billeci L, Pioggia G, Vaglini F, Ahluwalia A (2010) Automated extraction and classification of dynamic metrical features of morphological development in dissociated Purkinje neurons. *J Neurosci Methods* 185(2):315–324.
18. Caserta F, et al. (1995) Determination of fractal dimension of physiologically characterized neurons in two and three dimensions. *J Neurosci Methods* 56(2): 133–144.
19. Jelinek HF, Fernandez E (1998) Neurons and fractals: How reliable and useful are calculations of fractal dimensions? *J Neurosci Methods* 81(1-2):9–18.
20. Takeda T, Ishikawa A, Ohtomo K, Kobayashi Y, Matsuoka T (1992) Fractal dimension of dendritic tree of cerebellar Purkinje cell during onto- and phylogenetic development. *Neurosci Res* 13(1):19–31.
21. Lorenzetto E, et al. (2009) Genetic perturbation of postsynaptic activity regulates synapse elimination in developing cerebellum. *Proc Natl Acad Sci USA* 106(38): 16475–16480.
22. Miyazaki T, Hashimoto K, Shin HS, Kano M, Watanabe M (2004) P/Q-type Ca^{2+} channel α1A regulates synaptic competition on developing cerebellar Purkinje cells. *J Neurosci* 24(7):1734–1743.
23. Schikorski T, Stevens CF (1997) Quantitative ultrastructural analysis of hippocampal excitatory synapses. *J Neurosci* 17(15):5858–5867.
24. Teclemariam-Mesbah R, Wortel J, Romijn HJ, Buijs RM (1997) A simple silver-gold intensification procedure for double DAB labeling studies in electron microscopy. *J Histochem Cytochem* 45(4):619–621.

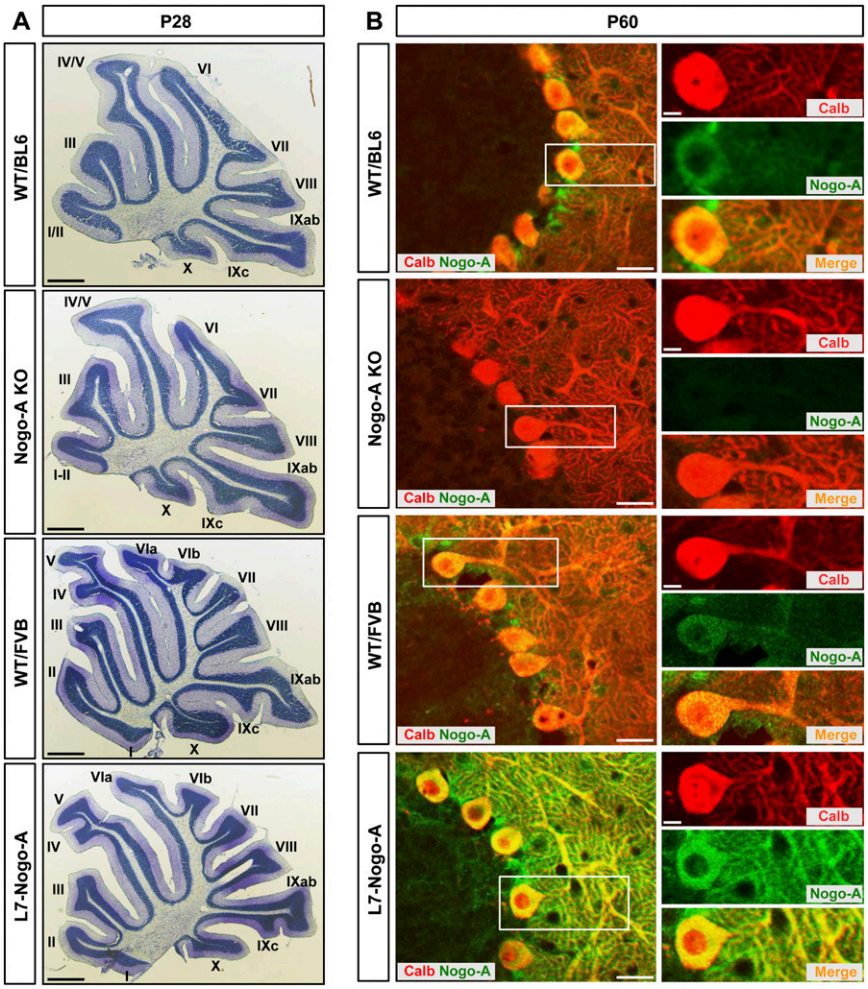

Fig. S1. Histological and immunohistochemical analysis of cerebella of wild-type and mutant mice. (*A*) Nissl-stained sagittal cerebellar sections from P28 Nogo-A KO, L7–Nogo-A TG, and corresponding WT mice. The lobule number is indicated by the numbers I–X. The cerebella of mutant mice show similar size, foliation, laminar organization, and histology to that of strain-matched control animals. (Scale bars, 300 μm.) (*B*) Expression of Nogo-A in the cerebellum of WT and mutant mice. Double immunolabeling with anti-calbindin (red) and anti–Nogo-A (green) antibodies revealed the low expression level of Nogo-A in PCs of adult (P60) WT mice of both strains, whereas it was highly expressed in PCs of L7–Nogo-A TG animals. Note the small calbindin^{-} but Nogo-A^{+} cells in the PC layer, which may correspond to candelabrum cells. Nogo-A was not detected in PCs of Nogo-A KO mice. Higher power micrographs correspond to the boxed regions. (Scale bars, 20 μm; 4 μm in the *Insets*.)

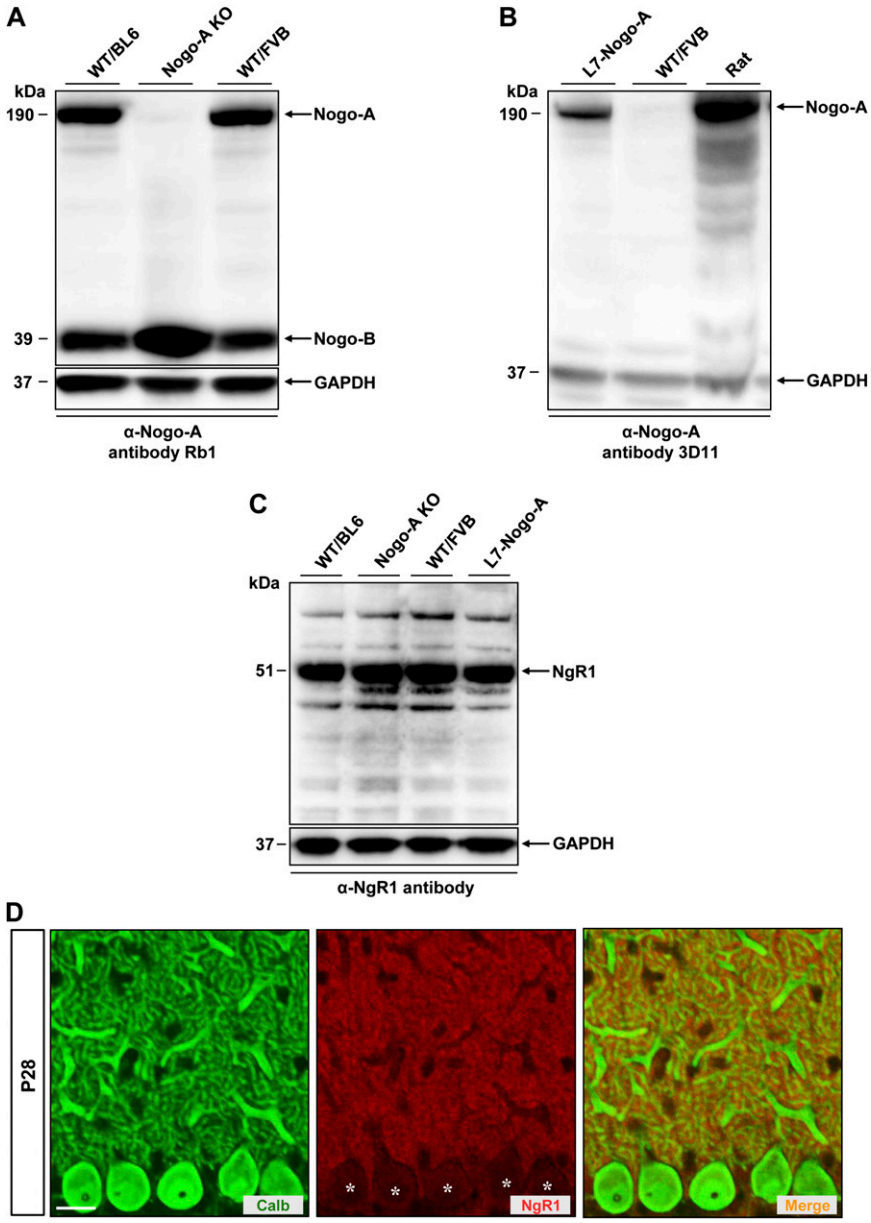

Fig. S2. Western blot analysis of Nogo-A and NgR1 expression in the cerebellar lysates of wild-type and mutant mice. (*A*) Immunoblotting with affinity-purified anti–Nogo-A antiserum Rb1 (Bianca) showing the expression of both Nogo-A and Nogo-B in the cerebella of P28 WT mice of C57BL/6 and FVB strain. A total of 30 μg of protein was loaded in each lane. Molecular markers are indicated on the *Left*. No difference in either Nogo-A or Nogo-B expression levels were detected due to the strain differences. This antibody shows no Nogo-A band in the Nogo-A KO cerebellar lysate, thus confirming its specificity. (*B*) Western blot analysis of a Nogo-A transgene expression in the cerebellar lysates (30 μg of protein per lane) of a P28 rat, WT/FVB, and L7–Nogo-A TG mice. In addition to confirming the presence of the transgene in the cerebellar lysates of L7–Nogo-A TG mice, the 3D11 antibody, specific for the rat Nogo-A, gave no detectable band in the cerebellar lysate of WT/FVB mice thus confirming its specificity. (*C*) Immunoblot analysis of NgR1 protein expression in cerebellar molecular layer lysates (30 μg per lane) of P28 Nogo-A KO, L7–Nogo-A TG, and the corresponding WT mice. No change in the amount of NgR1 protein was detected due to changes in the expression levels of Nogo-A. (*D*) Expression of NgR1 in the cerebellum of WT mice. Colabeling with anti-calbindin (green) and anti-NgR1 (red) antibodies revealed the high expression of NgR1 in the molecular layer and its very low expression in the PC bodies (stars) of P28 WT/BL6 mice. (Scale bar, 20 μm.)

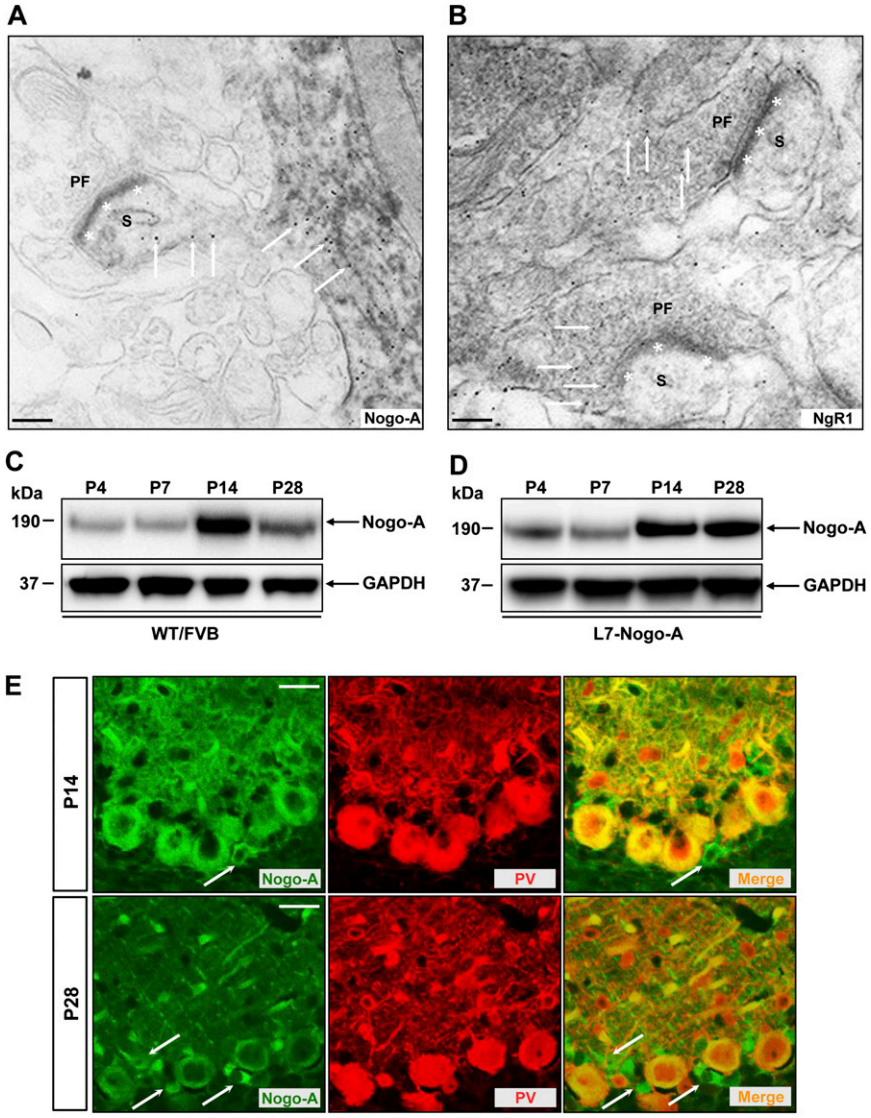

Fig. S3. Distribution of Nogo-A and NgR1 in the cerebellum. (*A* and *B*) Immunoelectron microscopic localization of Nogo-A and NgR1 in PF–PC synapses of P28 WT/BL6 mice. DAB staining was intensified with methenamine silver followed by gold substitution. Dark immunopositive staining for Nogo-A, intensified with silver-gold particles (arrows), is present in the postsynaptic PC dendritic spines (S) (*A*), whereas NgR1 immunolabeling, intensified with silver-gold particles (arrows), is confined to the presynaptic parallel fiber terminals (PF) (*B*). Stars demarcate postsynaptic densities. (Scale bars, 1 μm.) (*C* and *D*) Immunoblot analysis of Nogo-A expression during cerebellar development in WT/FVB and L7–Nogo-A TG mice. Western blot analysis of the cerebellar molecular layer lysates (30 μg of protein per lane) with monoclonal anti–Nogo-A antibody 11C7 shows that, in mice of both genotypes, Nogo-A reaches its peak of expression around P14 (*C* and *D*) and is afterward down-regulated in WT/FVB mice (*C*). In contrast, Nogo-A continues to be highly expressed in the molecular layer of L7–Nogo-A TG mice after P14, thus showing that the overexpression of Nogo-A under the L7 promoter starts only postnatally (*D*). (*E*) Expression of Nogo-A in the developing cerebellum of WT/BL6 mice. Double immunolabeling with anti–Nogo-A (green) and anti-parvalbumin (PV) (red) antibodies revealed the developmental down-regulation of Nogo-A protein expression in the PCs of WT/BL6 mice. The small, Nogo-A^{+} cells lined up along the PC-GC layer interface are most likely candelabrum cells, as suggested by their position and the lack of parvalbumin immunoreactivity (1). (Scale bars, 20 μm.)

1. Schilling K, Oberdick J, Rossi F, Baader SL (2008) Besides Purkinje cells and granule neurons: an appraisal of the cell biology of the interneurons of the cerebellar cortex. *Histochem Cell Biol* 130(4):601–615.

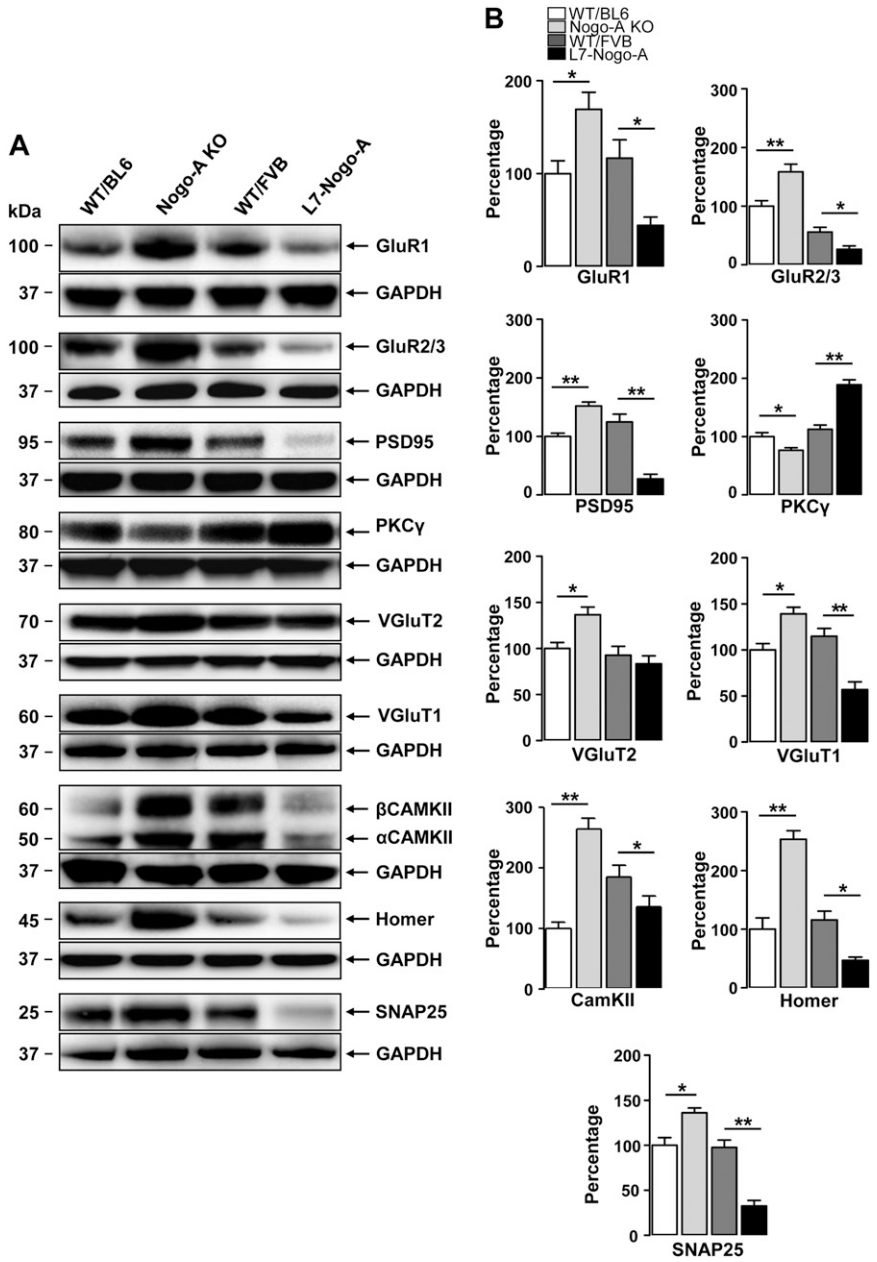

Fig. S4. Western blot analysis of GluR1, GluR2/3, PSD95, PKCγ, VGluT1, VGluT2, CamKII, Homer, and SNAP25 protein expression in the cerebellar lysates of wild-type and mutant mice. (*A*) Immunoblot analyses of GluR1, GluR2/3, PSD95, PKCγ, VGluT1, VGluT2, CamKII, Homer, and SNAP25 protein expression in the cerebellar molecular layer lysates (30 μg per lane) of P28 Nogo-A KO, L7–Nogo-A TG, and the corresponding WT mice. (*B*) The intensity of protein bands was quantified by densitometry and normalized to GAPDH protein used as a loading control, followed by normalization toward WT/BL6. Nogo-A negatively affects the expression levels of GluR1, GluR2/3, PSD95, VGluT1, CamKIIβ, Homer, and SNAP25, whereas the protein level of PKCγ is positively correlated with the amount of Nogo-A in PCs. Genetic deletion of Nogo-A resulted in an increase in the amount of the VGluT2, whereas overexpression of Nogo-A had no effect on the expression level of this protein. Values represent means ± SEM of three experiments repeated with three different animals per group; $*P < 0.05$, $**P < 0.01$, Student *t* test.

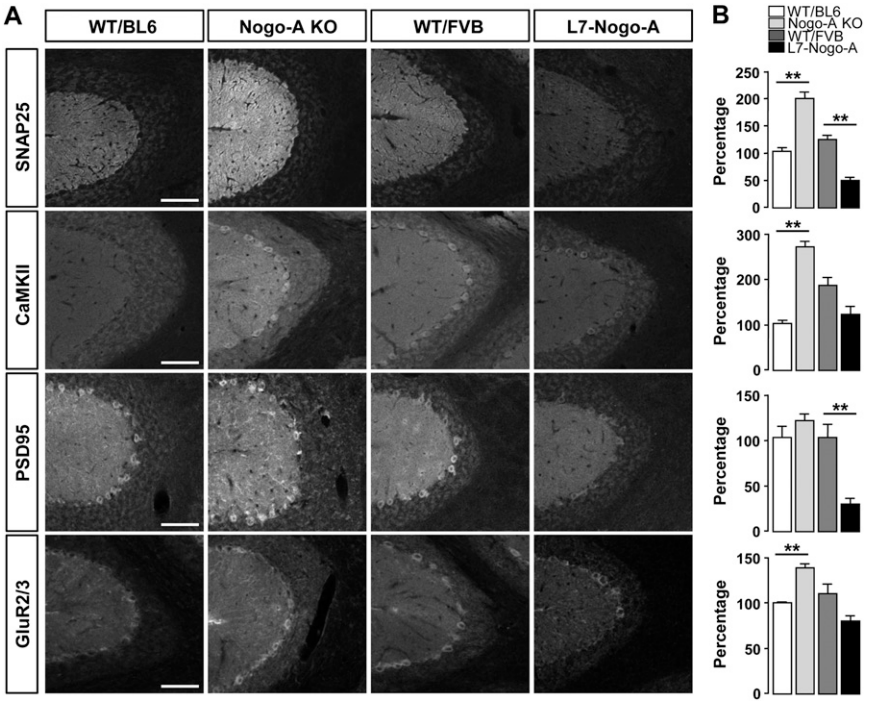

Fig. S5. Immunohistochemical analysis of SNAP25, CamKII, PSD95, and GluR2/3 protein expression in the cerebellar molecular layer of wild-type and mutant mice. (*A*) Expression pattern of SNAP25, CamKII, PSD95, and GluR2/3 in the cerebellar molecular layer of P28 Nogo-A KO, L7–Nogo-A TG, and corresponding WT mice. (Scale bars, 100 μm.) (*B*) The intensity of immunolabeling was quantified by densitometry and normalized toward WT/BL6 mice. The expression levels of SNAP25, CamKII, PSD95, and GluR2/3 are negatively correlated with the amount of Nogo-A. Values represent means ± SEM of three experiments repeated with three different animals per group; $^{**}P < 0.01$, Student *t* test.

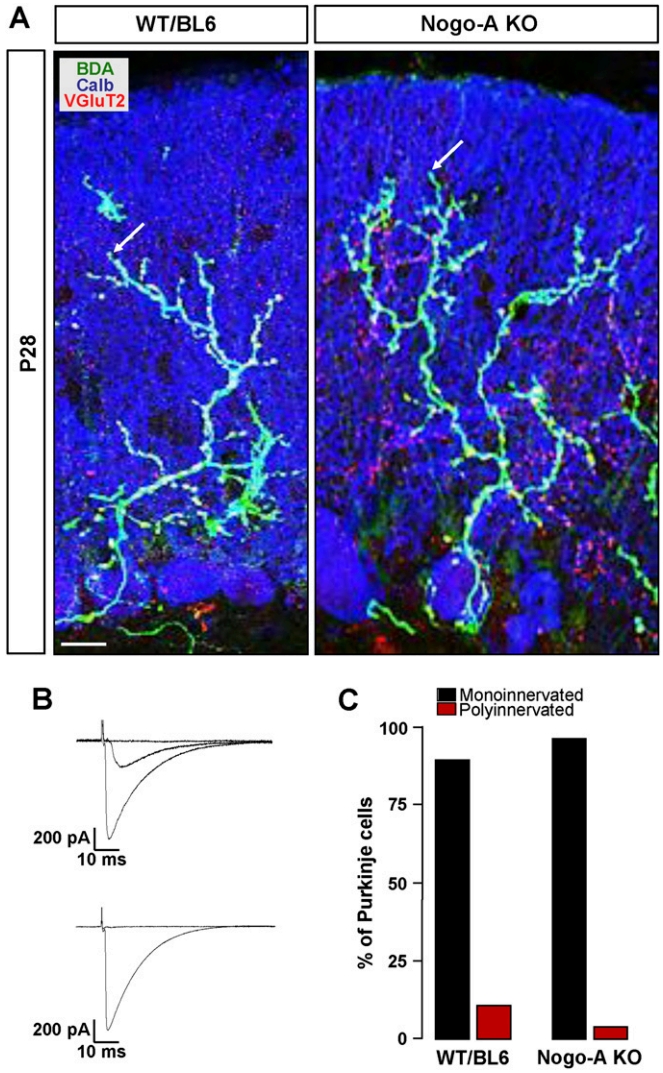

Fig. S6. Innervation pattern of Purkinje cells by climbing fibers at P28. (*A*) CF monoinnervation of Purkinje cells in P28 Nogo-A KO and WT/BL6 mice as revealed by a triple fluorescent labeling for calbindin (blue), BDA (green), and VGluT2 (red). In both Nogo-A KO ($n = 19$ cells from four mice) and control WT/BL6 ($n = 21$ cells from six mice) mice BDA-labeled CFs completely overlapped with $VGluT2^+$ CF terminals. Note also the increased CF innervation territory in Nogo-A KO mice (arrows). (Scale bar, 20 μm.) (*B*) Representative traces of EPSCs evoked by stimulation of poly- (*Upper*) and monoinnervated (*Lower*) CFs in the granule cell layer of P28 Nogo-A KO and WT/BL6 mice. Two to three traces are superimposed at each threshold stimulus intensity. Holding potential was −10 mV. (*C*) Summary histogram showing the percentage of mono- and polyinnervated PCs in P28 WT/BL6 ($n = 28$ cells from eight mice) and Nogo-A KO ($n = 30$ cells from seven mice) mice.

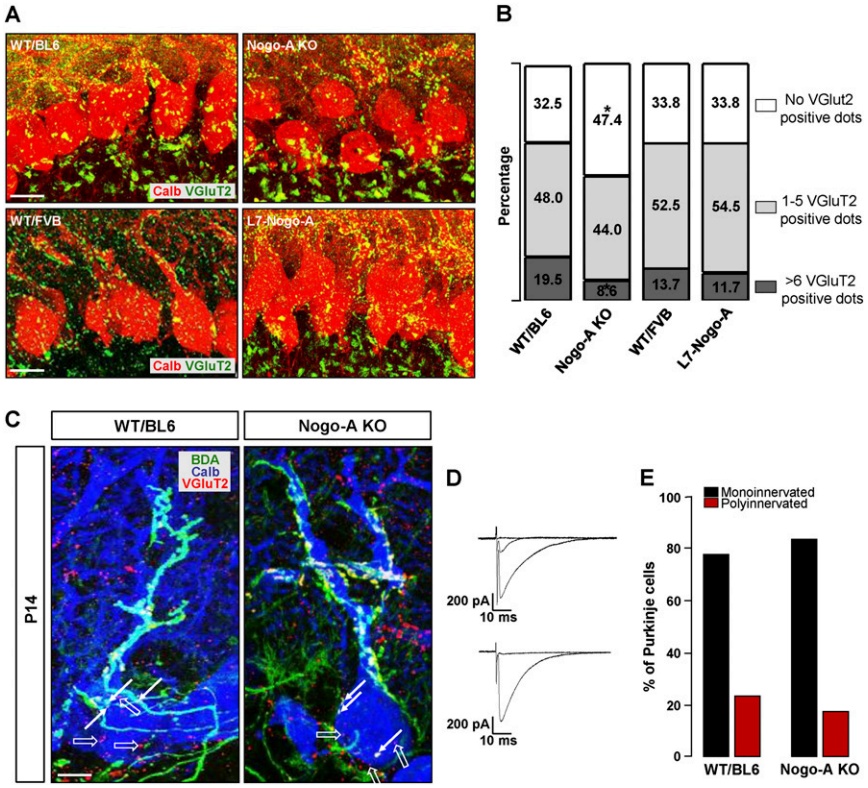

Fig. S7. Genetic deletion of Nogo-A affects the somatodendritic translocation of climbing fiber terminals. (*A*) Confocal images of VGluT2-labeled CF terminations (green) on P14 PCs stained for calbindin (red). (Scale bar, 20 μm.) (*B*) To estimate the translocation of CFs from the soma to dendrites of PCs, they were divided into three categories: PCs without VGluT2$^+$ CF varicosities on their soma, PCs with one to five VGluT2$^+$ CF terminals, and PCs with more than six VGluT2$^+$ CF varicosities. Genetic deletion of Nogo-A resulted in a faster translocation of CF synapses from PC bodies to their dendrites, whereas overexpression of Nogo-A had no effect on this process. Values represent means ± SEM of 120–132 cells (sampled from six mice) per genotype; *$P < 0.05$, Student *t* test. (*C*) CF innervation of PCs in P14 Nogo-A KO and WT/BL6 mice as revealed by a triple fluorescent labeling for calbindin (blue), BDA labeling of individual CF axons (green), and VGluT2 (red). Polyinnervated Nogo-A KO ($n = 21/102$ cells from four mice) and control WT/BL6 ($n = 24/92$ cells from five mice) PCs have comparable numbers of BDA$^+$/VGluT2$^+$ (arrows) and BDA$^-$/VGluT2$^+$ CF terminals (empty arrows) on their somata. (Scale bar, 5 μm.) (*D*) Representative traces of EPSCs evoked by the stimulation of poly- (*Upper*) and monoinnervated (*Lower*) CFs in the granule cell layer in WT/BL6 and Nogo-A KO mice at P14. Two to three traces are superimposed at each threshold stimulus intensity. Holding potential was −10 mV. (*E*) Summary histogram showing the percentage of mono- and polyinnervated PCs in P14 WT/BL6 ($n = 26$ cells from six mice) and Nogo-A KO ($n = 29$ cells from eight mice) mice.

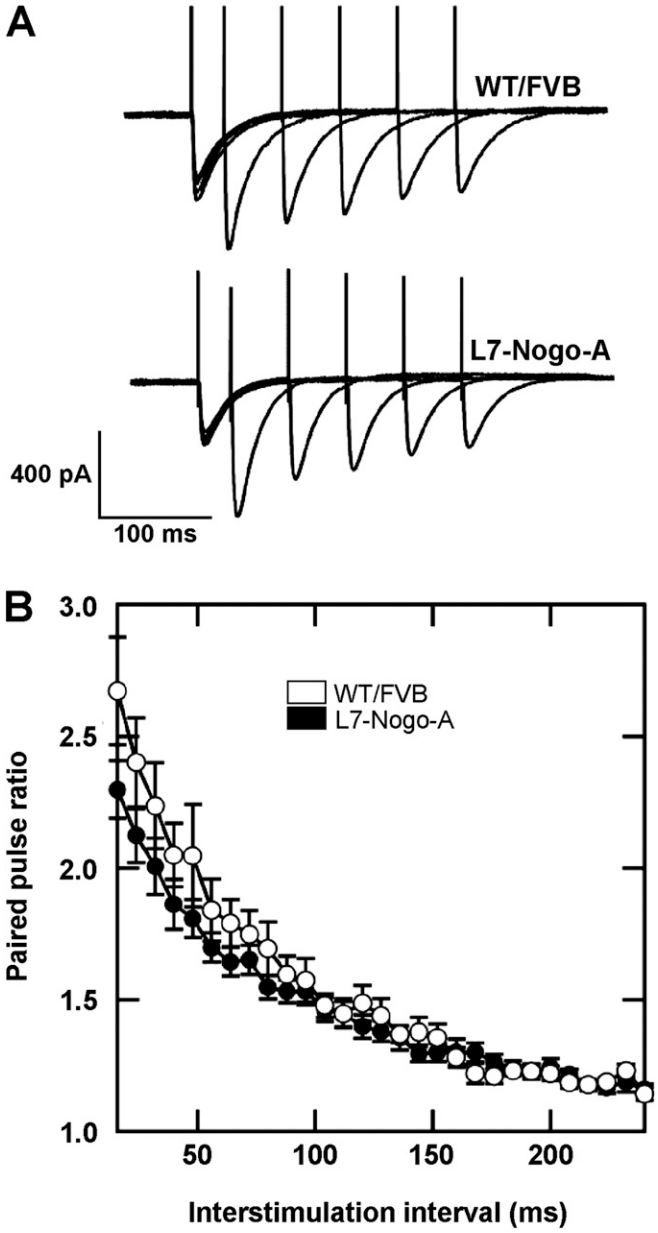

Fig. S8. Paired-pulse facilitation is not affected by Nogo-A overexpression. (*A*) Typical paired-pulse facilitation traces in L7–Nogo-A TG (P28) mice are indistinguishable from their WT controls. (*B*) Plotted values of paired-pulse facilitation ratio (the ratio was expressed as the difference between the second and the first EPSC divided by the size of the first EPSC) as a function of twin pulse interval. Overexpression of Nogo-A does not alter the probability of glutamate release from the presynaptic PFs. Values represent means ± SEM of 19–25 cells (sampled from four to five mice) per genotype; Student *t* test.